Ocean Science

Internal-tide vertical structure and steric sea surface height signature south of New Caledonia revealed by glider observations

Arne Bendinger[1,a], **Sophie Cravatte**[1,2], **Lionel Gourdeau**[1], **Luc Rainville**[3], **Clément Vic**[4], **Guillaume Sérazin**[4,b], **Fabien Durand**[1], **Frédéric Marin**[1], and **Jean-Luc Fuda**[5]

[1]Université de Toulouse, LEGOS (CNES/CNRS/IRD/UT3), Toulouse, France
[2]IRD, Centre IRD de Nouméa, New Caledonia
[3]Applied Physics Laboratory, University of Washington, Seattle, WA, USA
[4]Laboratoire d'Océanographie Physique et Spatiale, Univ. Brest, CNRS, Ifremer, IRD, IUEM, Brest, France
[5]Aix Marseille Univ., Université de Toulon, CNRS, IRD, MIO UM 110, Marseille, France
[a]now at: Laboratoire d'Océanographie Physique et Spatiale, Univ. Brest, CNRS, Ifremer, IRD, IUEM, Brest, France
[b]now at: Institut de Recherche de l'École Navale (IRENav), EA 3634 – École Navale, 29240, Brest, France

Correspondence: Arne Bendinger (arne.bendinger@univ-brest.fr)

Abstract. In this study, we exploit autonomous underwater glider data to infer internal-tide dynamics south of New Caledonia, an internal-tide-generation hot spot in the southwestern tropical Pacific. By fitting a sinusoidal function to vertical displacements at each depth using a least-squares method, we simultaneously estimate diurnal and semidiurnal tides. Our analysis reveals regions of enhanced tidal activity, strongly dominated by the semidiurnal tide. To validate our findings, we compare the glider observations to a regional numerical simulation that includes tidal forcing. This comparison assesses the simulation's realism in representing tidal dynamics and evaluates the glider's ability to infer internal-tide signals and their signature in sea surface height (SSH). The glider observations and a pseudo glider, simulated using hourly numerical model output with identical sampling, exhibit similar amplitude and phase characteristics along the glider track. Existing discrepancies are in large part explained by tidal incoherence induced by eddy–internal-tide interactions. We infer the semidiurnal internal-tide signature in steric SSH by the integration of vertical displacements. Within the upper 1000 m, the pseudo glider captures roughly 78 % of the steric SSH total variance explained by the full water column signal. This value increases to over 90 % when projecting the pseudo glider's vertical displacements onto climatological baroclinic modes and extrapolating to full depth. Notably, the steric SSH from glider observations aligns closely with empirical estimates derived from satellite altimetry, highlighting the internal tide's predominant coherent nature during the glider's sampling.

1 Introduction

Over the last 2 decades, in situ observations (e.g., Park and Watts, 2006; Zilberman et al., 2011; Nash et al., 2012; Vic et al., 2018), satellite altimetry (Ray and Zaron, 2016; Zhao et al., 2016; Zaron, 2019), and numerical modeling (for a review see Arbic et al., 2018; Arbic, 2022) have shed light on internal-tide dynamics at both regional and global scales. Important internal-tide-generation sites have been identified in regions such as the Hawaiian Islands, the Luzon Strait, the Indonesian seas, French Polynesia, the southwestern tropical Pacific, Madagascar, the Amazonian shelf break, and the Mid-Atlantic Ridge. At these locations, the barotropic tidal flow interacts with the bathymetry while radiating internal waves at tidal frequency into the stably stratified water column, expressed by vertical displacements of density surfaces (Bell Jr., 1975; Baines, 1982).

Each of the above tools, namely in situ observations, satellite altimetry, and numerical modeling, possesses its own set of benefits and limitations. In situ observations such as moorings provide excellent temporal resolution and in most cases

a sufficient vertical resolution to resolve the wave's vertical structure. However, these scattered in situ measurements are only representative at very local scales. Satellite altimetry provides a global view of internal tides, but long time series are needed, and the derived signal is mostly representative of low-vertical-mode dynamics at large horizontal scales. Numerical modeling overcomes both of these issues by investigating the fine spatial and temporal scales over a large region, although high-resolution grid spacing is needed, making numerical modeling computationally expensive. Further, these models and the underlying primitive equations may be simplifications of the complex reality that do not fully encapsulate the intricacies of the actual physical system. This concerns subgrid-scale physics such as unresolved dissipative effects which require parameterization through turbulent closure schemes. Generally, any interpretation and conclusion drawn from the above approaches should be taken with thoughtful consideration.

Among the in situ platforms, gliders have the potential to infer the vertical structure of internal tides while documenting their spatial variability. Traditionally used to document lower-frequency features such as mesoscale and submesoscale features at high spatial resolution (Rudnick, 2016; Testor et al., 2019), they have the potential to complement knowledge obtained from moorings and satellite altimetry. Commonly, gliders are programmed to provide subsurface observations by sampling the upper ocean in a sawtooth manner. For a maximum depth of 1000 m, a typical glider dive cycle is 6 h during which it travels 6 km horizontally. As they travel autonomously through the ocean over thousands of kilometers and for a duration on the order of months per mission, they can sample a large area. This makes gliders advantageous compared to other in situ platforms such as moorings, which are confined to fixed locations.

Glider measurements have been successfully exploited to sample hydrographic data at fine-scale resolution and to infer internal-tide dynamics in specific areas. Pioneer work using glider data was carried out by Rainville et al. (2013) and Johnston et al. (2013), who estimated the amplitude and phase of diurnal and semidiurnal internal tides. Glider data were shown to capture the phase propagation away from the generation site and map the mode-1 energy flux at Luzon Strait. Johnston and Rudnick (2015) extracted diurnal and semidiurnal internal tides from repeated glider cross-shore transects in the California Current system. They link the internal-tide-induced mixing with elevated diffusivity estimates. Johnston et al. (2015) revealed standing wave patterns in the Tasman Sea as incident mode-1 internal tides reflected on the continental slope. Moreover, internal tides were extracted from gliders that were employed for vertical profiling, serving as fixed-point time series while remaining stationary (Hall et al., 2017, 2019). However, inferring internal tides from glider measurements is challenging due to the smearing of temporal variability into spatial variability. This makes it difficult to separate high-frequency signals from low-frequency (but spatially varying) motions such as mesoscale and submesoscale features (Rudnick and Cole, 2011; Rainville et al., 2013).

This study focuses on internal tides south of New Caledonia, an internal-tide-generation hot spot in the southwestern tropical Pacific (Fig. 1), recently described and quantified in Bendinger et al. (2023) using numerical modeling. Internal-tide generation was found to be closely linked with the north–south stretching ridge system composed of shelf breaks, oceanic ridges, and seamounts, which represent a major obstacle for the barotropic tidal flow bending around New Caledonia. In the full regional domain, a total of 15.27 GW is converted from the barotropic to the baroclinic M2 tide, comparable to well-known sites of enhanced energy conversion in the Pacific Ocean such as the Hawaiian Ridge (Merrifield et al., 2001; Merrifield and Holloway, 2002; Carter et al., 2008). Barotropic-to-baroclinic energy conversion is associated with the main bathymetric structures, namely Grand Passage, Pines Ridge, Norfolk Ridge, and Loyalty Ridge (see Fig. 1), governed by the semidiurnal M2 tide and strongly dominated by mode 1. Tidal energy propagation is characterized by well-confined tidal beams that diverge away from the generation hot spots north and south of New Caledonia with depth-integrated energy fluxes of up to 30 kW m^{-1} in the annual mean.

The above model analysis only concerned the coherent tide, which is the stationary component being constant in amplitude and phase (Ray and Zaron, 2016; Zhao et al., 2016; Zaron, 2019). The departure from tidal coherence is referred to as tidal incoherence, i.e., the temporally varying amplitude and phase within the tidal frequency band. It is characterized by its unpredictability often linked to mesoscale variability and stratification changes both close to the generation site and during tidal energy propagation (Zhao et al., 2010; Kerry et al., 2014; Buijsman et al., 2017; Zaron, 2017). Particularly, mesoscale turbulence and background currents were shown to cause a tidal beam refraction associated with changing phase speeds and, consequently, alterations in the propagation of internal tides (Rainville and Pinkel, 2006; Duda et al., 2018; Guo et al., 2023).

From an in situ perspective, the numerical model results remain to be fully validated. In situ observations of fine-scale physics in the region are rare. Moored measurements of velocity were used to compare kinetic energy frequency spectra with the numerical model output (Durand et al., 2017; Bendinger et al., 2023). However, the mooring is located neither close to a pronounced internal-tide-generation site nor in the propagation direction. Insight into fine-scale dynamics around New Caledonia is given by a unique set of glider surveys undertaken in the period from 2011 to 2014 (Durand et al., 2017). One of these glider missions surveyed the region of high internal-tide activity south of New Caledonia, which is also a region of high mesoscale eddy activity (Keppler et al., 2018) and submesoscale activity (Sérazin et al., 2020). Disentangling balanced from unbalanced mo-
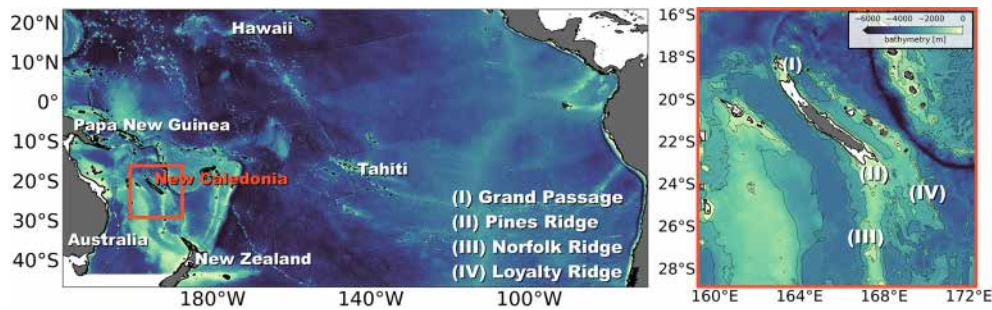
Figure 1. The location of New Caledonia in the southwestern tropical Pacific is shown in the left panel, an area characterized by complex bathymetry with continental shelves, shelf breaks, large- and small-scale ridges, and seamounts. Bathymetry (shading) is taken from Bendinger et al. (2023). The red box outlines the region of interest, which is zoomed in on the right panel, highlighting the major bathymetric features, i.e. (I) Grand Passage, (II) Pines Ridge, (III) Norfolk Ridge, and (IV) Loyalty Ridge, subject to strong internal-tide generation. The thin black lines represent the 1000, 2000, and 3000 m depth contours. The thick black line is the 100 m depth contour representative of the New Caledonian lagoon.

tions (mesoscale and submesoscale features from internal waves) in this area is a challenge of particular interest in the context of the Surface Water Ocean Topography (SWOT) satellite altimetry mission (launched in December 2022) and the SWOT Adopt-A-Crossover (AdAC) initiative (d'Ovidio et al., 2019; Morrow et al., 2019). SWOT provides high-resolution sea surface height (SSH) measurements along two swaths of 60 km width, each resolving wavelengths down to 15 km, which is up to 10 times higher resolution than conventional altimetry (Fu et al., 2012; Ballarotta et al., 2019; d'Ovidio et al., 2019; Morrow et al., 2019). The availability of three-dimensional in situ observations may provide insight into the SSH expression of fine-scale dynamics, with important implications for disentangling SWOT SSH measurements. New Caledonia represents an interesting site for addressing mesoscale and submesoscale SSH observability in a region with strong internal tides. Specifically, the glider data can be very useful in linking the vertical structure of the ocean interior with the ocean surface. Although not suitable for the direct assessment of SWOT, it represents an important in situ dataset with relevant information about the governing dynamics at play.

This study's objective lies in the exploitation of the glider's spatiotemporal sampling in the upper 1000 m to infer internal-tide dynamics, including their steric SSH signature south of New Caledonia. To assess our findings, we seek a complementary validation of the regional numerical simulation by glider observations and vice versa. On the one hand, the glider observations will assess the realism of internal tides' simulation in the regional model. On the other hand, the regional model will address the capability of the methodologies applied to the glider observations. Specifically, we address the following questions. How do the observation-based and simulated internal-tide fields compare with each other? Can observations and the model be used complementarily to deduce tidal coherence and tidal incoherence? To

what extent are the glider observations of the upper 1000 m sufficient to deduce the internal-tide steric SSH signature?

2 Data

2.1 Glider observations

This study focuses on autonomous Spray glider observations obtained during a mission from 12 August to 23 October 2014 within a series of glider surveys around New Caledonia in the framework of the Southwest Pacific Ocean Circulation and Climate Experiment (SPICE; Ganachaud et al., 2014; Durand et al., 2017). The glider surveyed continuously temperature and salinity with respect to pressure in the upper 1000 m as it traveled horizontally and vertically in the water column while sending its GPS location before each descending and after each ascending profile (Fig. 2).

Along the glider's path, a total of 560 (ascending/descending) profiles were analyzed which were acquired over the course of 73 d and a horizontal travel distance of 1150 km. The glider track as a function of days since deployment is shown in Fig. 3. The glider was deployed at the southern edge of the New Caledonian lagoon at 166° E, 22° S before heading south to 26.5° S and heading back north to its initial starting position. The mean duration of a glider profile is 2.9 h (3.4 h for the mean descending profile, 2.4 h for the mean ascending profile). The mean horizontal displacement is 2.1 km (2.4 km for the mean descending profile, 1.7 km for the mean ascending profile). Aborted glider profiles as well as profiles featuring faulty GPS data were discarded from the analysis. The acquired glider time series of temperature and salinity with respect to pressure were divided into descending and ascending profiles by allocating the glider time stamp with the maximum dive depth. The profiles were then vertically gridded and binned in 10 m depth intervals.
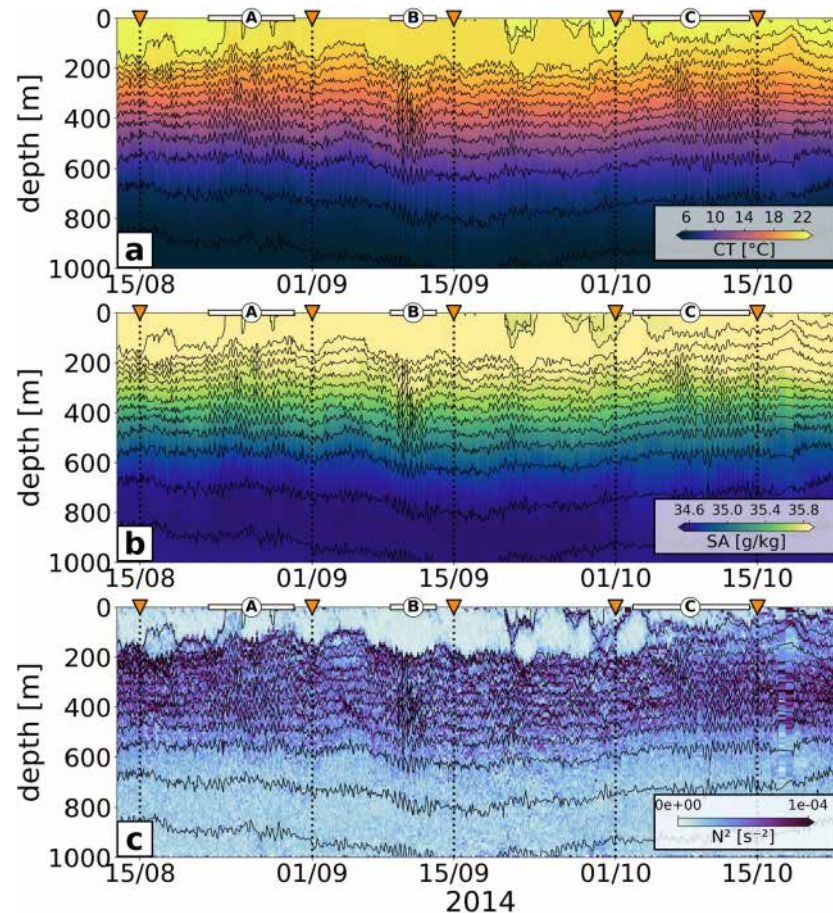
Figure 2. Glider observations' **(a)** conservative temperature (CT), **(b)** absolute salinity (SA), and **(c)** squared buoyancy frequency (N^2) overlaid by potential density contours and gridded in 10 m bins along the vertical axis. The orange triangles (and the dotted vertical lines) mark the glider waypoints as given in Fig. 3. The white bars represent the sections of potential tidal beam crossing, namely A, B, and C (as defined in Fig. 3).

While ascending profiles experience clean flow, descending profiles may be distorted, inter alia, due to wake turbulence linked to the glider wing's attack angle ($3°$). Descending profiles were found to feature a mean salinity offset at mid-depths ($\sim 0.04\,\mathrm{g\,kg^{-1}}$), where the density gradient is strongest. This salinity offset vanishes near the surface and 1000 m depth. Even though we expect physically driven high-frequency variability between descending and ascending profiles, the salinity differences should be centered around zero for glider dives that are randomly distributed during various phases of the tides. Considering a mean salinity gradient of $0.025\,\mathrm{g\,kg^{-1}\,m^{-1}}$ at mid-depths, the salinity offset would correspond to a vertical displacement of less than 2 m, which is much smaller than the internal-tide-driven signal shown below. In the following, we will regard the salinity offset as negligible. Furthermore, we point out that having both descending and ascending profiles is crucial for our methodology to ensure a sufficient number of data points at mid-depth to fit high-frequency internal-tide variability (see Sect. 3.1).

2.2 Numerical simulation

This study uses numerical output of a model configuration that consists of a host grid (TROPICO12; $1/12°$ horizontal resolution and 125 vertical levels) and covers the tropical and subtropical Pacific Ocean basin from $142°$ E–$70°$ W and $46°$ S–$24°$ N (Fig. 1), as presented in Bendinger et al. (2023). The oceanic reanalysis GLORYS2V4 prescribes initial conditions for temperature and salinity as well as the forcing with daily currents, temperature, and salinity at the open lateral boundaries. ERA5 produced by the European Centre for Medium-Range Weather Forecasts (ECMWF; Hersbach et al., 2020) provides atmospheric forcing at hourly temporal resolution and a spatial resolution of $1/4°$ to compute surface fluxes using bulk formulae and the model prognostic sea surface temperature. The model is forced by the tidal potential of the five major diurnal (K1, O1) and semidiurnal (M2, S2, N2) tidal constituents. At the open lateral boundaries it is forced by barotropic sea surface height and barotropic currents of the same five tidal constituents taken
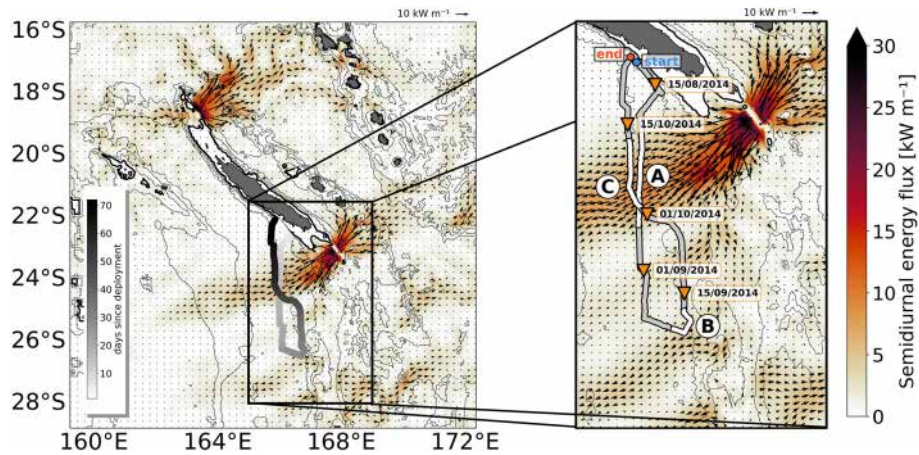
Figure 3. CALEDO60 regional model domain showing the depth-integrated coherent semidiurnal energy flux (shading) including flux vectors and the glider track of the glider mission south of New Caledonia as a function of days since deployment. The inset zooms in on the study area. For the sake of better visualization and orientation, orange triangles and the associated time stamps mark waypoints along the glider track (15 August, 1 September, 15 September, 1 October, and 15 October 2014). The highlighted white segments (A, B, C) illustrate potential major crossings of glider track and tidal beam energy propagation.

from the global tide atlas FES2014 (Finite Element Solution 2014; Lyard et al., 2021). A higher-resolution horizontal grid is nested within the host grid in the southwestern tropical Pacific Ocean encompassing New Caledonia (Fig. 3). This nesting grid features $1/60°$ horizontal resolution or ~ 1.7 km grid box spacing initialized by an Adaptive Grid Refinement in Fortran (AGRIF; Debreu et al., 2008). AGRIF was explicitly designed for the Nucleus for European Modelling of the Ocean (NEMO) to set up regional simulations embedded in a predefined model configuration. Further, it enables the two-way lateral boundary coupling between the host and the nesting grid during the whole length of the simulation.

Bendinger et al. (2023) illustrated the model's eligibility of realistically simulating both background ocean dynamics (i.e., large-scale circulation, kinetic energy spectra) and tidal dynamics. Briefly, the regional circulation characterized by westward zonal jets and boundary currents alongside the spatial pattern of eddy kinetic energy levels were found to be well simulated. Kinetic energy levels are very close to in situ observations on the mesoscale to submesoscale as well as inertial to tidal timescales. The modeled internal-tide dynamics have been validated in terms of barotropic-to-baroclinic energy conversion against semianalytical theory, showing good agreement when considering conversion rates on subcritical slopes only. In addition, the internal tide's surface signature has been validated against satellite altimetry, revealing reasonable amplitude and large-scale patterns.

Here, we focus on the model year 2014 using the hourly regional model output (CALEDO60) of the three-dimensional velocity field, temperature, salinity, and pressure. This model output was also subject to a coherent tidal analysis at each grid point, providing the tidal harmonics for the diurnal and semidiurnal constituents as well as tidal energetics. The

harmonic analysis constraint to a full calendar year relies upon a compromise between high computational expenses and the representative extraction of the coherent tide through a time series long enough to sample a representative variability in the mesoscale turbulent field. The annual-mean depth-integrated semidiurnal coherent energy flux for the regional model domain is shown in Fig. 3, suggesting that the glider crossed several times an area of pronounced westward internal-tide energy propagation, characterized by narrow tidal beams. The temporal overlap of glider observations and numerical model output allows for a complementary assessment of both datasets.

2.3 Geostrophic surface currents

We used altimetry-derived global ocean gridded maps $(1/4°)$ of geostrophic surface currents from absolute dynamic topography, generated and processed by the EU Copernicus Marine Environment Monitoring Service (CMEMS). We used the multimission Data Unification and Altimeter Combination System (DUACS) product in delayed time and at daily resolution with all satellite missions available at a given time. We extracted geostrophic surface currents for the glider period of August–October 2014, which served as input for the ray tracing in Sect. 3.5.

2.4 HRET

The internal-tide-induced SSH signature along the glider track is computed using empirical estimates from the High Resolution Empirical Tide product (HRET version 8.1; Zaron, 2019). This product uses essentially all exact repeat altimeter mission data during a 25-year-long time series of SSH observations (1992–2017, TOPEX/Jason, Geosat, ERS,

Envisat). Based on a point-wise harmonic analysis along all available satellite tracks and a plane-wave fit in overlapping patches, it provides the coherent amplitude and phase for the major semidiurnal (M2, S2) and diurnal (K1, O1) tides for modes 1–3. Here, we reconstruct the coherent semidiurnal time series of SSH along the glider track direction using the M2 and S2 harmonics for modes 1–2 to compare with the glider-derived steric height (Sect. 2.4).

3 Methods

3.1 Glider-derived internal-tide amplitude and phase in 3 d running windows

The amplitude and phase of internal tides, derived from glider observations with irregular sampling in both space and time, are determined using a well-established methodology from Rainville et al. (2013). This methodology relies on the sinusoidal regression of vertical (isopycnal) displacements in 3 d running windows using a least-squares fit. The choice of the 3 d window is ultimately linked to a compromise between (1) a minimum time series length that captures the diurnal period between 18 and 36 h and the semidiurnal period between 10.3 and 14.4 h, (2) an adequate number of tidal cycles within 3 d for the statistical analysis, and (3) a time period during which the internal-tide amplitude and phase do not vary significantly during the glider's horizontal displacement. In our case, the corresponding travel distance over 3 d is approximately 50 km. The vertical displacement is computed as follows:

$$\eta = g \frac{\sigma_s - \overline{\sigma}}{\sigma_s \overline{N^2}}, \qquad (1)$$

where g is the gravitational acceleration; σ_s is the sample density; and $\overline{\sigma}$ and $\overline{N^2}$ are the mean density and mean squared buoyancy frequency relative to the 3 d running window, respectively. Further, a linear trend was subtracted which we attribute to sloping isopycnals of low-frequency motion. Following Rainville et al. (2013), we fit simultaneously the K1 ($\omega_d = 2\pi/23.9345 \, \text{h}^{-1}$) and M2 ($\omega_{sd} = 2\pi/12.4206 \, \text{h}^{-1}$) internal tide for each depth layer and each 3 d time window, i.e.,

$$\eta(t, z) = A_d(z) e^{(-i w_d t + \phi_d(z))} + A_{sd}(z) e^{(-i w_{sd} t + \phi_{sd}(z))}, \qquad (2)$$

where A_d and A_{sd} are the diurnal and semidiurnal amplitude, respectively. Equivalently, ϕ_d and ϕ_{sd} are the diurnal and semidiurnal phases. Here, the phase is relative to the Unix epoch (00:00:00 UTC on 1 January 1970). Note that even though we solve for the peak frequencies of the K1 and M2 tides, the fitted amplitude and phase are representative of the diurnal and semidiurnal frequency band since the 3 d window does not allow for a separation among the diurnal or semidiurnal tidal constituents. The sampling of the glider observations, the underlying methodology to extract the diurnal

and semidiurnal tide, and the overall workflow are illustrated and summarized in the schematic in Fig. 4.

The sinusoidal fit for the diurnal and semidiurnal internal tide applied to the glider observations is explicitly shown for a 3 d window in Fig. 5. Explained variability γ is here given by the following covariances: $\text{cov}(\eta_d, \eta)/\text{var}(\eta)$ for the diurnal fit with the diurnal internal-tide-induced vertical displacement η_d and $\text{cov}(\eta_{sd}, \eta)/\text{var}(\eta)$ for the semidiurnal fit with the semidiurnal internal-tide-induced vertical displacement η_{sd}. In this example, the measured signal is governed by a semidiurnal cycle, captured well by the sinusoidal fit and explaining 77 % of the total variance. The diurnal signal is rather weak in amplitude and barely contributes to the total variance (1 %). The residual signal accounts for 22 %. Note that the 3 d window might be too narrow to distinguish between diurnal and near-inertial signals ($\omega_{NI} = 2\pi/29.4819 \, \text{h}^{-1}$ at 24° S). However, the vertical displacements induced by the diurnal tide and near-inertial motion are significantly reduced compared to the dominant semidiurnal tide, as shown further below. Overall, the methodology gives us confidence in our ability to accurately reconstruct the amplitude and phase of the internal tide south of New Caledonia.

3.2 Full-model pseudo-glider simulation

The temporal overlap of glider observations and numerical simulation output is a great opportunity to compare in situ observations and the regional simulation. To do so, we simulate what we call a full-model pseudo glider by extracting the model's three-dimensional and hourly output for conservative temperature, salinity, and pressure (see middle panel in Fig. 4). The variables are then interpolated onto the glider track with the same irregular spatiotemporal sampling as the glider observations, followed by the division into descending and ascending profiles and the gridding in vertical 10 m bins. Moreover, diurnal and semidiurnal amplitude and phase are determined just as in the glider observations by applying a sinusoidal fit to vertical displacements in 3 d running windows. In this way, we create pseudo-glider-like observations mimicking the glider mission with the full-model variability.

3.3 Coherent pseudo-glider simulation

In this study we build upon a harmonic analysis performed on the full-model output for each grid point in the regional model domain as described in Bendinger et al. (2023). Briefly, the objective is to obtain a reference dataset from a modeling perspective for the coherent internal-tide amplitude and phase along the glider track. We refer to this as the coherent pseudo glider. The methodology is presented in the following and illustrated in the bottom panel in Fig. 4. The coherent internal-tide-induced amplitude and phase of vertical displacements are deduced from the three-dimensional
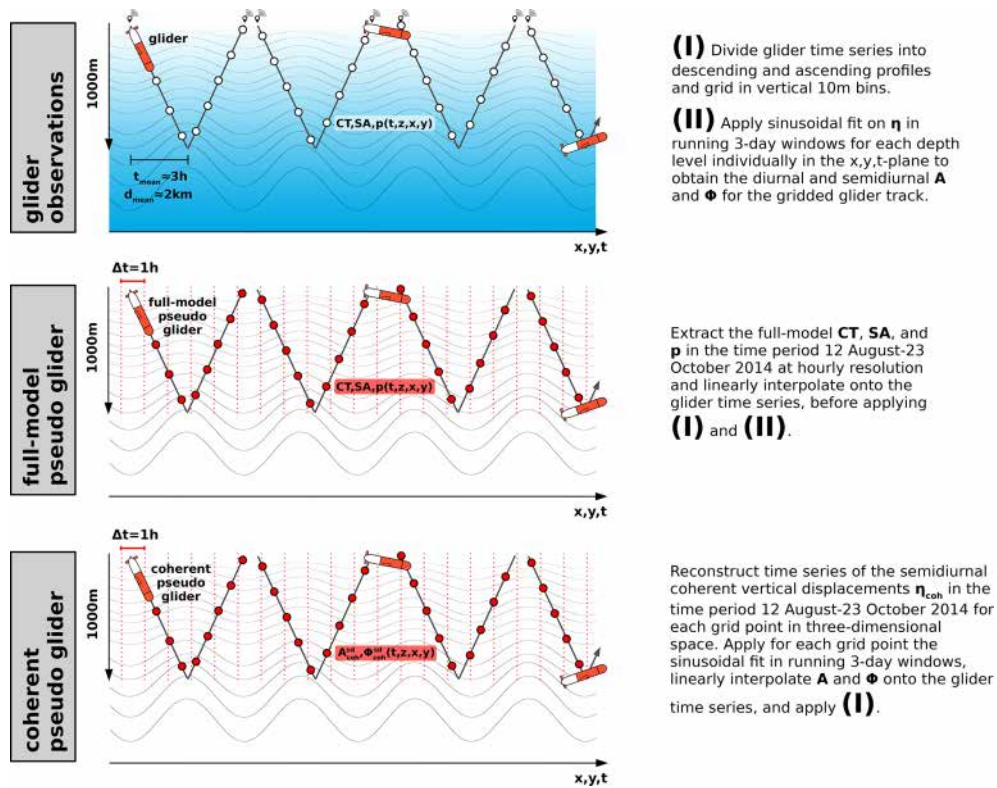
Figure 4. Schematic for the glider observations (top panel), the full-model pseudo glider (middle panel), and the coherent pseudo glider (bottom panel). Note that the full-model pseudo glider and the coherent pseudo-glider sampling are identical to the one in the glider observations, i.e., the sampling considers the horizontal displacement during the glider profile as a function of time. This is achieved by linearly interpolating the model hourly output onto the glider time series.
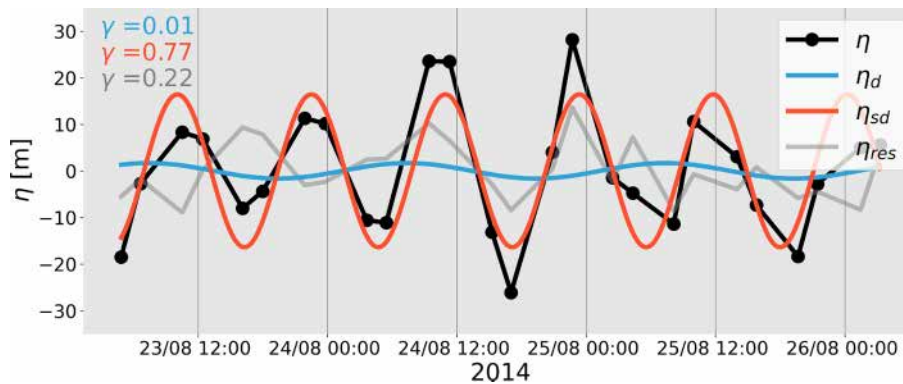

Figure 5. Glider-observation-derived vertical displacements (black, η) for an exemplary 3 d window at 300 m depth and the sinusoidal fit of the diurnal (blue, η_d) and semidiurnal (red, η_sd) internal tide and the residual signal (gray, η_res). The respective explained variability γ is also shown.

baroclinic vertical velocity harmonic as follows:

$$\eta_\mathrm{coh}(z) = \frac{w_\mathrm{A}(z)T}{2\pi}, \tag{3}$$

where w_A is the harmonically fitted amplitude of vertical velocity for each grid point in the domain and T is the respective tidal period. Note that here we only consider the semidiurnal coherent internal tide since it is largely dominant over

the diurnal tide, as shown further below. The semidiurnal coherent vertical displacements are computed by reconstructing a time series for each semidiurnal tidal constituent (i.e., M2, S2, N2) using w_A and the harmonically fitted phase w_Φ before summing over the three time series to obtain the semidiurnal time series $\eta_\mathrm{coh}^\mathrm{sd}$ for each grid point in three-dimensional space. Once reconstructed, we apply the sinusoidal fit in 3 d

running windows just as we did for the glider observations but for each grid point. We obtain the semidiurnal coherent amplitude $A_{\text{coh}}^{\text{sd}}$ and phase $\Phi_{\text{coh}}^{\text{sd}}$ in three-dimensional space at hourly resolution. Finally, we interpolate $A_{\text{coh}}^{\text{sd}}$ and $\Phi_{\text{coh}}^{\text{sd}}$ onto the glider track with the same irregular spatiotemporal sampling as the glider observations, followed as above by the division into descending and ascending profiles and the gridding in vertical 10 m bins. We computed the semidiurnal coherent amplitude and phase for both the total baroclinic signal (modes 1–9) and mode 1.

3.4 Climatological vertical modes

We computed climatological vertical mode profiles for vertical velocity and displacement along the glider track to infer the modal structure of the glider and the pseudo-glider vertical displacements (see Sect. 3.6.1). Climatological modes are computed by solving the Sturm–Liouville eigenvalue problem (Gill, 1982):

$$\frac{\partial^2 \Phi_n}{\partial z^2} + \frac{N^2}{c_n^2}\Phi_n = 0, \tag{4}$$

where Φ is the eigenfunction describing the vertical structure for vertical velocity or displacement subject to the boundary conditions $\Phi(0) = \Phi(-H) = 0$, n is the mode number, and c_n is the separation constant. We solve the eigenvalue problem for climatological profiles of stratification N inferred from climatological profiles of conservative temperature and absolute salinity taken from the CSIRO Atlas of Regional Seas (CARS) for each glider profile location (Ridgway et al., 2002). For this study's purpose, the climatological modes were averaged along the glider track and cut to a representative depth of 3000 m, which is being considered the full-depth range below.

3.5 Ray tracing

A ray-tracing method following Rainville and Pinkel (2006) is used to infer the departure from tidal coherence in the glider observations or full-model pseudo glider, associated with the refraction of the tidal beam due to mesoscale background currents, i.e., mesoscale eddies. Specifically, the horizontal propagation of internal gravity modes is investigated considering spatially varying topography, climatological stratification, planetary vorticity, and depth-independent currents. Following this approach, we assume that departure from tidal coherence is primarily due to varying background currents. The choice of depth-independent currents relies on the general assumption that mesoscale eddies are well represented by a barotropic and a mode-1 baroclinic structure with limited vertical shear (Smith and Vallis, 2001). Also, the assumption of considering only depth independence is validated a posteriori, given the relevance of the qualitative picture of ray trajectories that are obtained.

Bathymetry is taken from ETOPO2v2 (Smith and Sandwell, 1997). Internal gravity wave speeds are predefined and solved by the Sturm–Liouville problem for stratification from the World Ocean Atlas (Locarnini et al., 2018; Zweng et al., 2019). We model semidiurnal ray paths for modes 1–2, initialized at the internal-tide-generation hot spot south of New Caledonia near Pines Ridge (167.65° E, 23.35° S) and for a given propagation angle (southwestward; 210°). In an iterative procedure, the ray tracing considers for each step size (1 km) bathymetry, climatological buoyancy and planetary vorticity effects, and the background currents. Through the dispersion relation from the Helmholtz equation for internal wave modes assuming a local wave expression, the ray's group and phase velocity are obtained, which are then used to update the ray's position and direction (angle of propagation). To mimic the effects of background currents on the ray's path, a no-current scenario is also given. The ray tracing is applied on two different velocity products: (1) the depth-averaged currents as derived from the daily-mean three-dimensional velocity field from the regional model output (CALEDO60) and (2) the geostrophic surface currents as derived from CMEMS. For the latter, the depth-independent currents are approximated by multiplying the SSH-derived geostrophic surface currents by a factor of 0.5, following Rainville and Pinkel (2006). Note that the ray-tracing results of (1) and (2) are rather qualitative. The two data products used in the ray tracing contain different dynamics. Specifically, the gridded two-dimensional fields from CMEMS do not resolve the same spatial and temporal scales as CALEDO60. Thus, the direct comparison of the ray tracing needs to be taken with caution.

3.6 Internal-tide-induced steric height

To our knowledge, glider observations have never been used to derive the SSH signature of fine-scale dynamical structures such as internal tides. In the following, we introduce the methodology to derive the SSH signature, i.e., steric height, of internal tides using glider data limited to the upper 1000 m. Further, the available data in the upper 1000 m are exploited to account for the internal-tide steric height signal at depths beyond 1000 m and, thus, for the full-depth range.

3.6.1 Glider and pseudo-glider steric height

Following Zhao et al. (2010), we deduce the steric height h of internal tides from surface pressure p_{surf}, i.e., the vertical integral of vertical displacements η:

$$h(t) = \frac{1}{\rho_0 g}\rho_0 \underbrace{\int_{-H}^{0} N^2(z,t)\eta(z,t)\mathrm{d}z}_{p_{\text{surf}}(t)}, \tag{5}$$

where H is the ocean depth. Since the glider observations are limited to the upper 1000 m depth, Eq. (5) becomes

$$h_{\text{obs}}^{1000\,\text{m}}(t) = \frac{1}{\rho_0 g}\rho_0 \underbrace{\int_{1000\,m}^{0} N^2(z,t)\eta_{\text{obs}}^{1000\,\text{m}}(z,t)\text{d}z}_{p_{\text{surf}}^{1000\,\text{m}}(t)}, \quad (6)$$

where $h_{\text{obs}}^{1000\,\text{m}}$ is the glider steric height and $\eta_{\text{obs}}^{1000\,\text{m}}$ is the glider vertical displacement. Since glider measurements for a given profile are not instantaneous and are associated with different time stamps, we interpolated the vertical displacements onto a common time stamp (t_{glider}) that represents the glider's time stamp at mid-depths (see the schematic in Fig. 6). This is achieved by interpolating the reconstructed time series, utilizing amplitude and phase data from the sinusoidal fit, onto the respective t_{glider} of the profile.

Additionally, we explore steric height inferred by a modal projection of glider vertical displacements on a set of climatological modes followed by an extrapolation to the full-depth range. The objective is to understand to what extent Eq. (6) and, thus, the vertical integral limited to glider measurements in the upper 1000 m are a sufficient approximation to account for the surface signature of internal tides. Further, we investigate whether we could infer the surface signature with a better accuracy assuming that internal tides are well represented by the modal structure of modes 1–2.

Using a least-squares fitting method, we project the glider vertical displacements onto a set of climatological modes, as obtained from Sect. 3.4 and limited to the upper 1000 m:

$$\eta_{\text{obs}}^{1000\,\text{m}}(z,t) = \sum_{n=1}^{2} \widetilde{\eta}_{n,\text{obs}}^{1000\,\text{m}}(t)\Phi_n^{1000\,\text{m}}(z). \quad (7)$$

For each time step, the least-squares solution is then used to extrapolate to the full-depth range using the regression coefficient $\widetilde{\eta}_{n,\text{obs}}^{1000\,\text{m}}$ and the full-depth climatological mode Φ_n^{full} to obtain the full-depth glider vertical displacements $\eta_{\text{obs}}^{\text{full}}$. In this study the glider vertical displacements are projected using a maximum of two modes (two-mode approximation). The projection on the first mode only is referred to as first-mode approximation. The associated steric height for the full-depth range was computed equivalent to above:

$$h_{\text{obs}}^{\text{full}}(t) = \frac{1}{\rho_0 g}\rho_0 \underbrace{\int_{-H}^{0} N^2(z)\eta_{\text{obs}}^{\text{full}}(z,t)\text{d}z}_{p_{\text{surf}}^{\text{full}}(t)}, \quad (8)$$

where $h_{\text{obs}}^{\text{full}}$ is referred to as the full-depth glider steric height. Similarly, we compute pseudo-glider steric height $h_{\text{pseudo}}^{1000\,\text{m}}$ and the full-depth pseudo-glider steric height $h_{\text{pseudo}}^{\text{full}}$ as deduced from $\eta_{\text{pseudo}}^{1000\,\text{m}}$ and $\eta_{\text{pseudo}}^{\text{full}}$, respectively.

3.6.2 Full-model steric height

To have a ground truth for the internal-tide surface signature for the full-depth range, we computed steric height from the regional model output as follows:

$$h_{\text{model}}^{\text{full}} = \int_{-H}^{\eta_0} \delta(z)\rho_0\text{d}z, \quad (9)$$

where $\rho_0 = 1035\,\text{kg m}^{-3}$ is the reference density, η_0 is the free surface displacement, and δ is the specific volume anomaly. The latter is computed as

$$\delta(z) = \frac{1}{\rho(\text{CT}, \text{SA}, z)} - \frac{1}{\rho(\text{CT}_{\text{ref}}, \text{SA}_{\text{ref}}, z)}, \quad (10)$$

with CT_{ref} and SA_{ref} the reference conservative temperature (0 °C) and the reference absolute salinity (standard ocean reference salinity, $35.16504\,\text{g kg}^{-1}$). The steric anomaly was computed for each grid point from vertical profiles of conservative temperature and absolute salinity. The steric SSH is then obtained through vertical integration before being bandpassed in the semidiurnal frequency band and interpolated onto the time stamps representative of the glider profiles along the glider track (t_{glider} in Fig. 6). The full-depth steric height $h_{\text{model}}^{\text{full}}$ is compared with the full-depth pseudo-glider steric height $h_{\text{pseudo}}^{\text{full}}$. In addition, we also computed the steric height contribution in the upper 1000 m, i.e.,

$$h_{\text{model}}^{1000\,\text{m}} = \int_{1000\,\text{m}}^{\eta_0} \delta(z)\rho_0\text{d}z, \quad (11)$$

which serves for the comparison with the pseudo-glider steric height $h_{\text{pseudo}}^{1000\,\text{m}}$.

4 Results

In the following, we first explore the glider observations, the underlying dominance, and spatiotemporal variability in the semidiurnal internal tide before comparing these with the model. The pseudo-glider simulation is then used to link the ocean interior with the ocean surface by investigating the extent to which the upper 1000 m vertical displacements are sufficient to determine the steric height signal of internal tides.

4.1 Semidiurnal internal-tide dominance

The simultaneous fit of vertical displacements η for the diurnal and semidiurnal tide for the upper 1000 m along the whole glider section, expressed by the explained variance of the total signal, is presented in Fig. 7. The field is overwhelmingly dominated by the semidiurnal tide along the entirety of the section and throughout the water column from 100–200 m below the surface down to 1000 m depth. Locally, the
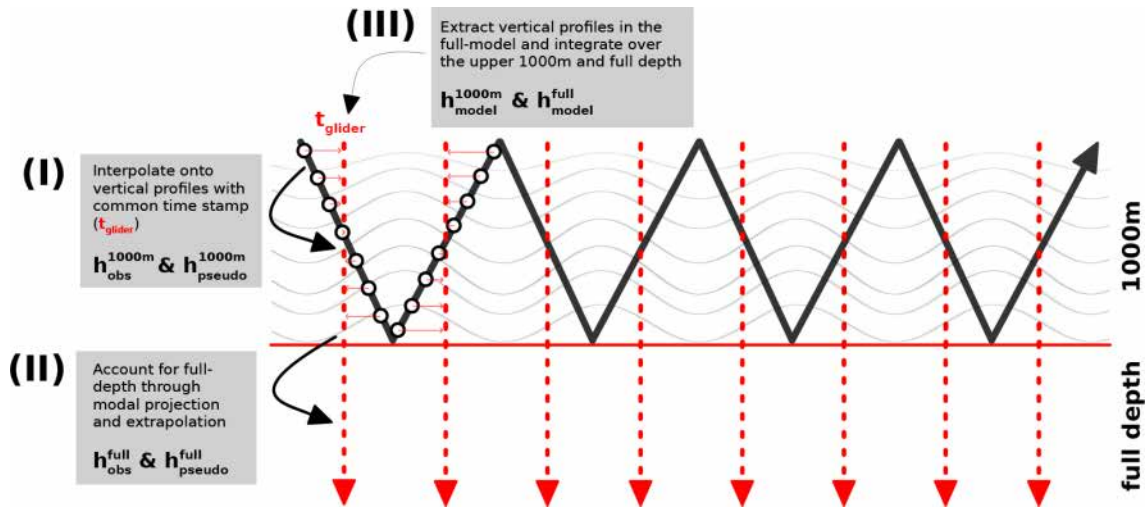
Figure 6. Schematic illustrating (I) the linear interpolation of vertical displacements for a given profile onto a common time stamp t_{glider} prior to the vertical integration to obtain $h_{\text{obs}}^{1000\,\text{m}}$ and $h_{\text{pseudo}}^{1000\,\text{m}}$, (II) the modal projection on climatological modes and extrapolation to the full-depth range to obtain $h_{\text{obs}}^{\text{full}}$ and $h_{\text{pseudo}}^{\text{full}}$, and (III) the vertical extraction in the full model at t_{glider} to obtain $h_{\text{model}}^{1000\,\text{m}}$ and $h_{\text{model}}^{\text{full}}$.
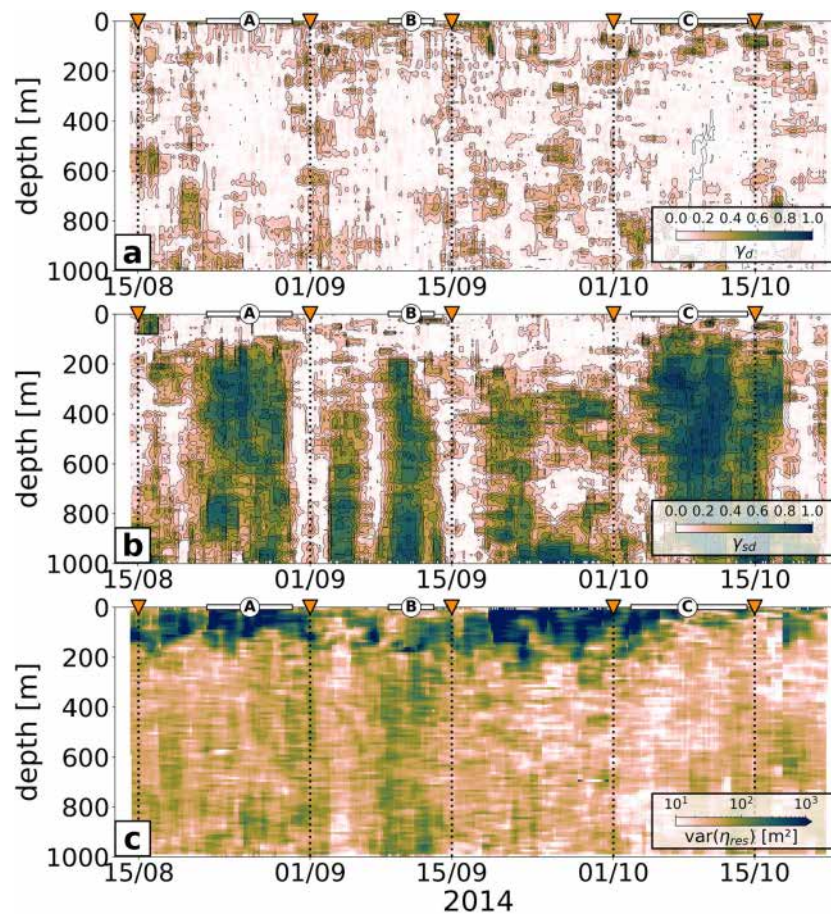
Figure 7. Explained variance by the **(a)** diurnal ($\gamma_{\text{d}} = \text{cov}(\eta_{\text{d}}, \eta)/\text{var}(\eta)$) and **(b)** semidiurnal ($\gamma_{sd} = \text{cov}(\eta_{sd}, \eta)/\text{var}(\eta)$) internal tide as given by the sinusoidal fit applied on the glider observations. **(c)** Variance of the residual signal $\text{var}(\eta_{\text{res}})$.

semidiurnal displacement variance explains up to 80 % of the total displacement variance (Fig. 7b). The diurnal tide is of a rather patchy nature and explains less than 10 % of the whole signal most of the time (Fig. 7a). The residual signal stands out as it features high variance near the surface in the upper 100–200 m, while diurnal and semidiurnal signals are weak. This corresponds to expectations; i.e., vertical displacements of low-mode baroclinic tides are zero at the surface and weak in the upper layers. Further, the mixed layer near the surface represents a complex flow regime with a broad variety of dynamics; i.e., internal-tide-induced vertical displacements are no longer the dominant signal. Considering that the fit is performed over a period of 3 d and a horizontal distance of 50 km, the residual may be linked to surface-intensified submesoscale dynamics. In the upper ocean, near-inertial motion may also contribute to the residual signal. We theoretically estimated the near-inertial vertical displacements at a given latitude with an a priori knowledge of their kinetic energy referenced to the semidiurnal vertical displacements through the ratio of kinetic energy (KE) to potential energy (PE) for inertial gravity waves following Gill (1982):

$$\frac{\text{KE}}{\text{PE}} = \frac{\omega^2 + f^2}{\omega^2 - f^2}. \tag{12}$$

With PE being proportional to $\eta^2 N^2$; i.e., for semidiurnal tides $\text{PE}_{\text{sd}} \propto \eta_{\text{sd}}^2 N^2$ and near-inertial waves $\text{PE}_{\text{ni}} \propto \eta_{\text{ni}}^2 N^2$, this results in

$$\frac{\eta_{\text{ni}}}{\eta_{\text{sd}}} = \left(\frac{\text{KE}_{\text{ni}}}{\text{KE}_{\text{sd}}} \frac{\omega_{\text{ni}}^2 - f^2}{\omega_{\text{ni}}^2 + f^2} \frac{\omega_{\text{sd}}^2 + f^2}{\omega_{\text{sd}}^2 - f^2} \right)^{1/2}. \tag{13}$$

The ratio $\frac{\text{KE}_{\text{ni}}}{\text{KE}_{\text{sd}}} \leq 10^{-1}$ is estimated by the horizontal kinetic energy power spectrum (not shown). With $f = 5.92 \times 10^{-5}\,\text{s}^{-1}$, $\omega_{\text{ni}} = 1.05 - 1.15 f$, and $\omega_{\text{sd}} = 1.405 \times 10^{-4}\,\text{s}^{-1}$, this gives a range of $\frac{\eta_{\text{ni}}}{\eta_{\text{sd}}} = 0.08 - 0.14$. This corresponds to a range of $\eta_{\text{ni}} = 1.2 - 2.1\,\text{m}$, which is not only smaller than the semidiurnal displacements ($\eta_{\text{sd}} = 15\,\text{m}$) but also smaller than the observed residual (see Fig. 5). Further, the residual should be linked to anything which is not semidiurnal, not diurnal, and to a large extent not near-inertial as the diurnal and near-inertial signals partly overlap in the 3 d window fits.

In the following, we will only focus on the semidiurnal internal tide since it represents the dominant signal in the region. This is also in agreement with Bendinger et al. (2023), which attributed 96 % of the barotropic-to-baroclinic energy conversion in their regional model domain to the semidiurnal tide (M2, S2, N2).

4.2 Spatiotemporal variability in semidiurnal internal tide: in situ observations vs. numerical model

The spatiotemporal variability in the semidiurnal internal tide is investigated in the following (Fig. 8). The glider observations reveal strong spatiotemporal variability during the > 2-month glider survey, as shown by the semidiurnal amplitude (Fig. 8a) and phase (Fig. 8e). Along the glider track, there are distinct patterns of enhanced semidiurnal tide amplitude (> 20 m) corresponding to large fractions of explained variability (see Fig. 7b).

Based on the modeling results, these patterns are localized to the most distinct tidal beams (labeled as A, B, and C). At these locations, semidiurnal tidal energy propagates westward, which can be traced back to the formation or superposition of tidal beams to the south of New Caledonia (Fig. 3). The pronounced southwestward-propagating tidal beam is crossed twice: on the way south in late August (A) and when heading back north in early to mid-October (C) towards the coast of New Caledonia. A third distinct tidal beam worth mentioning is encountered when the glider changes its heading direction from southward to northward (B). Another double crossing of tidal beams (but with weaker amplitudes) is observed in early September and from the middle to end of September, also visible in the depth-integrated semidiurnal energy flux (Fig. 3).

Glider observations and the full-model pseudo glider show an overall similarity in the spatiotemporal variability. Specifically, this applies to the location, the magnitude, and the vertical structure/extent of the tidal beams (Fig. 8a and e for the glider observations and Fig. 8b and f for the full-model pseudo glider).

Differences between the observations and the full-model pseudo glider are most evident in mid-August and early October. During these periods, we find strong tidal signatures in the full-model pseudo glider expressed by elevated amplitudes of isopycnal displacements. This is also apparent from the fitted phase. Given that both glider observations and the full-model pseudo glider feature identical sampling, variations linked to the spring and neap tide cycle are not valid hypotheses. Potential sources for the discrepancies may lie in the erroneous representation of the model's bathymetry and stratification leading to inaccuracies in simulating the precise beam location or the model's vertical mode structure. However, the bathymetry product used has received careful attention in the model configuration and is believed to accurately represent fine-scale bathymetric features, while stratification was validated against climatology (Bendinger et al., 2023). Another contributing factor is tidal incoherence, which can arise from eddy–internal-tide interactions, i.e., temporally varying background currents. Mesoscale and submesoscale features are by nature stochastic. Particularly, mesoscale and submesoscale eddies are not expected to be found at similar locations and times in reality and in the numerical simulation. The semidiurnal internal tide as derived from glider observations and the full-model pseudo glider appears to a large extent to have a coherent nature when taking the coherent pseudo glider as a reference dataset (Fig. 8c, g). The tidal signatures in mid-August and early October in the full-model pseudo glider are a clear exception. In the subsequent section, we explore whether discrepancies in the mesoscale
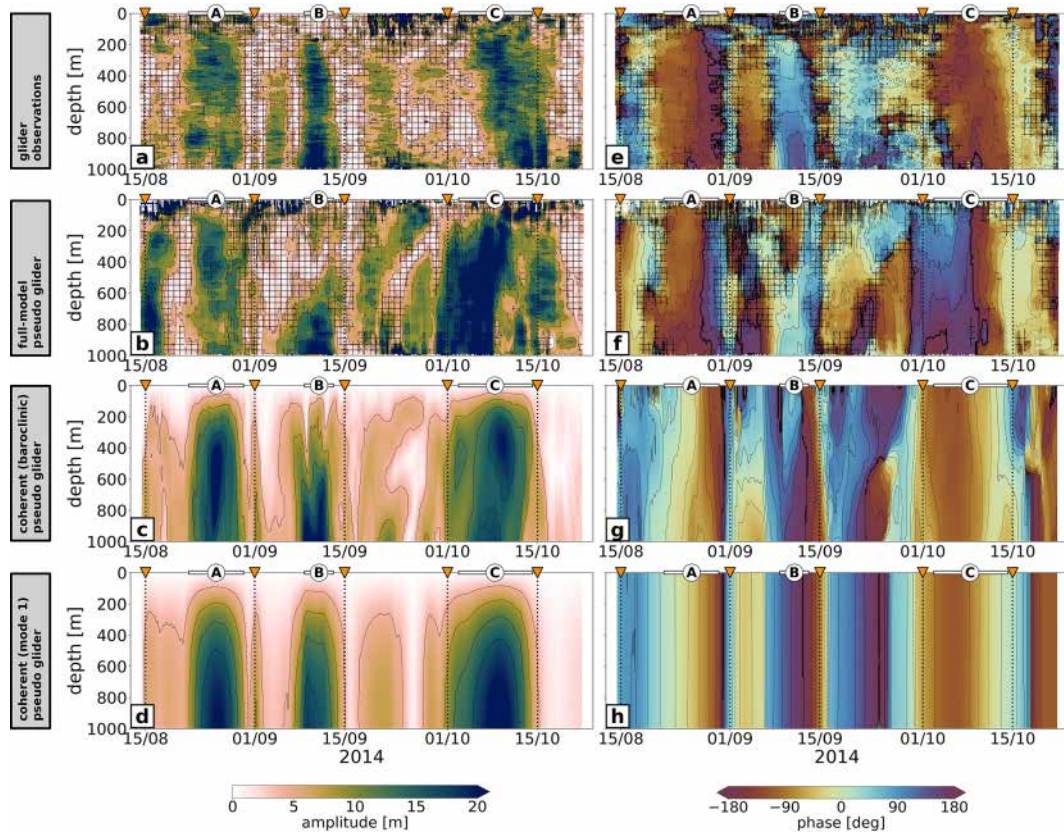
Figure 8. Semidiurnal amplitude for **(a)** glider observations, **(b)** the full-model pseudo glider, and **(c)** the coherent pseudo glider. **(d)** Same as **(c)** but for vertical mode 1. **(e)**–**(f)** Same as **(a)**–**(d)** but for the semidiurnal phase. Hatches in **(a)**–**(b)** and **(e)**–**(f)** represent areas where the residual signal explains more than twice the variance of the semidiurnal fit.
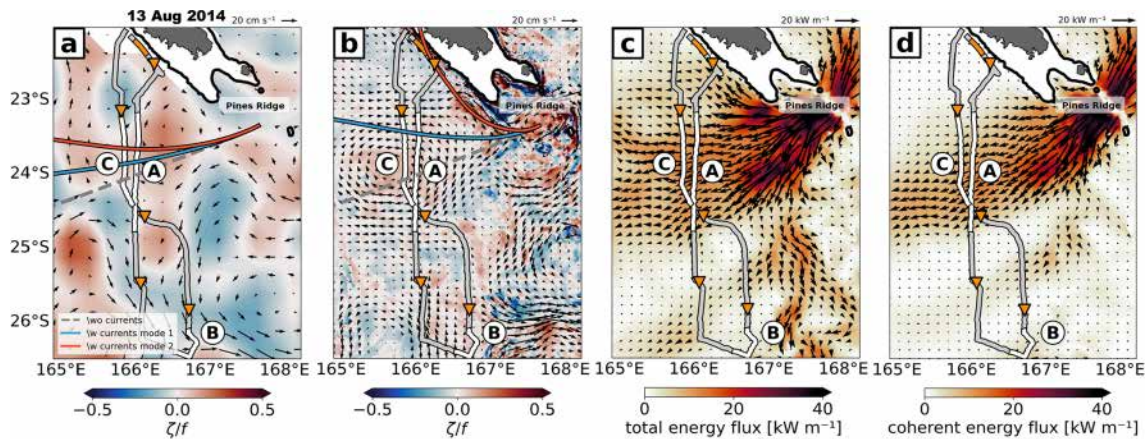

Figure 9. Zoom of the glider study site showing **(a)** the geostrophic surface currents (vectors) as obtained from satellite altimetry (CMEMS) with the underlying relative vorticity normalized by f (shading) for a daily-mean snapshot on 13 August 2014. **(b)** Same as **(a)** but showing the depth-averaged currents as obtained from CALEDO60. Also shown is the modeled **(c)** total semidiurnal energy flux and **(d)** coherent semidiurnal energy flux for a daily-mean snapshot on 13 August 2014. The ray-tracing results in **(a)** and **(b)** show the theoretical ray path of a semidiurnal tidal beam for mode 1 (blue) and mode 2 (red) that initiate from the generation site south of New Caledonia close to Pines Ridge. The no-current scenario is also given (dashed gray). The orange triangles are as in Fig. 3. The glider position and the distance covered on 13 August 2014 are shown by the highlighted orange bar along the glider track. The thick black line is the 100 m depth contour representative of the New Caledonian lagoon.

background field offer insights into differences observed in the sampled semidiurnal internal-tide field.

4.3 Tidal incoherence inferred from pseudo-glider simulations

To infer the impact of mesoscale eddies on the tidal beam's refraction and corresponding incoherence, we apply a simplified ray tracing following Rainville and Pinkel (2006) (see Sect. 3.5). We initiate a semidiurnal ray just west of Pines Ridge, which is known as a hot spot of internal-tide generation (Bendinger et al., 2023). The theoretical ray paths for modes 1–2 are shown for two different snapshots on 13 August 2014 (Fig. 9) and 3 October 2014 (Fig. 10). The background velocity field is clearly different between glider observations and the full-model pseudo glider for both snapshots. The no-current scenario is by definition the same since it relies on the same climatological stratification, bathymetry, and planetary vorticity. The semidiurnal ray propagates southwestward, corresponding to the well-confined propagation direction of the coherent tidal beam. Including the background currents introduces differing ray paths between glider observations and the full-model pseudo glider, as explored next.

On 13 August 2014, the mesoscale eddy field as given by satellite-altimetry-derived geostrophic surface currents has only a small impact on the semidiurnal ray path, though it is slightly refracted northward. Mode 2 is more affected than mode 1 (Fig. 9a). This contrasts with the numerical simulation, which is characterized by a mesoscale cyclone close to the New Caledonian coast and Pines Ridge and which quickly refracts the semidiurnal ray northward (Fig. 9b). This aligns with the modeled semidiurnal energy flux along the western New Caledonian coast (Fig. 9c) and corresponds to the full-model pseudo-glider sampling at the start of the section in mid-August (see Fig. 8b, f).

On 3 October 2014, the ray tracing provides a similar picture (Fig. 10). Even though a mesoscale anticyclone governs the background velocity field in the satellite altimetry observations, the tidal beam orientation is barely affected (Fig. 10a). Further, it is refracted equatorward, away from the glider sampling, and is therefore not captured by the glider observations in early October (see Fig. 8a, e). This is in contrast to the numerical simulation, in which a predominant anticyclone is located just off the New Caledonian coast and Pines Ridge (Fig. 10b). In the propagation direction, the semidiurnal rays are increasingly refracted southward (poleward) with increasing distance to the initialization region as they pass through the mesoscale eddy. Again, mode 2 is more affected than mode 1. Particularly, the theoretical beam is refracted toward the full-model pseudo-glider sampling location, providing a possible explanation for the premature detection of the tidal beam in early October (see Fig. 8b, f), which in the no-current scenario is predicted at a later stage $O(1\,\mathrm{d})$ along the glider track.

From an in situ perspective, the glider observations have provided a first insight into the spatiotemporal variability in the internal tide south of New Caledonia. Largely dominated by the semidiurnal tide and especially mode 1, the glider observations also highlight the realism of internal tides in the regional numerical simulation in the upper 1000 m. We conclude that major discrepancies between glider observations and the full-depth pseudo glider are not associated with deficiencies in the glider sampling or the model's realism of simulating internal tides but rather with tidal incoherence. Here, we showed that tidal incoherence is largely dependent on the background eddy field. In the following, we attempt to derive how the vertical structure of the semidiurnal internal tide in the upper 1000 m is expressed in the steric SSH signature.

4.4 To what extent can we use gliders to account for internal-tide-induced steric height?

The ability of the glider to retrieve the steric SSH signature of the semidiurnal tide is investigated using the regional numerical simulation only. We first use the full-model pseudo-glider simulation to evaluate the limitations due to the depth extent of the glider measurements. We compare (1) steric height inferred from the semidiurnal vertical displacements within the upper 1000 m only $\left(h_{\mathrm{pseudo}}^{1000\,\mathrm{m}}\right)$ with (2) steric height inferred from the semidiurnal vertical displacements in the upper 1000 m extrapolated to the full depth using projections on climatological modes 1–2 $\left(h_{\mathrm{pseudo}}^{\mathrm{full}}\right)$. To evaluate the errors in steric SSH reconstruction arising from the irregular glider sampling, we finally use the full-model steric SSH, which is free of any glider-like sampling. We remind the reader that the full-model steric SSH was initially computed from vertical profiles of specific volume anomaly, integrated over the water column, bandpassed in the semidiurnal frequency band, and interpolated onto the glider's profile location and time stamp at mid-depth. It can be regarded as ground truth for steric SSH within the upper 1000 m $\left(h_{\mathrm{model}}^{1000\,\mathrm{m}}\right)$ and the full-depth range $\left(h_{\mathrm{model}}^{\mathrm{full}}\right)$. They are respectively confronted with $h_{\mathrm{pseudo}}^{1000\,\mathrm{m}}$ and $h_{\mathrm{pseudo}}^{\mathrm{full}}$ to assess the glider's ability to deduce steric SSH (see Sect. 3.6). Note that we exclude in the following analysis the near-surface ocean layer, i.e., the upper 100 m, which might be contaminated by mixed-layer dynamics and mesoscale to submesoscale dynamics expressed by the elevated residual in Fig. 7c.

We first analyze $h_{\mathrm{model}}^{\mathrm{full}}$ along the glider track (Fig. 11a). The semidiurnal internal tide is expressed in steric height with magnitudes of up to 5 cm. It is primarily associated with the locations that have been identified as segments of elevated tidal activity (A, B, C in Figs. 3 and 8). The overwhelming majority of the semidiurnal steric SSH, i.e., 91 % $\left(h_{\mathrm{model}}^{1000\,\mathrm{m}}\right)$, is attributed to the contribution of internal-tide vertical displacements in the upper 1000 m (Fig. 11a–b and Table 1).
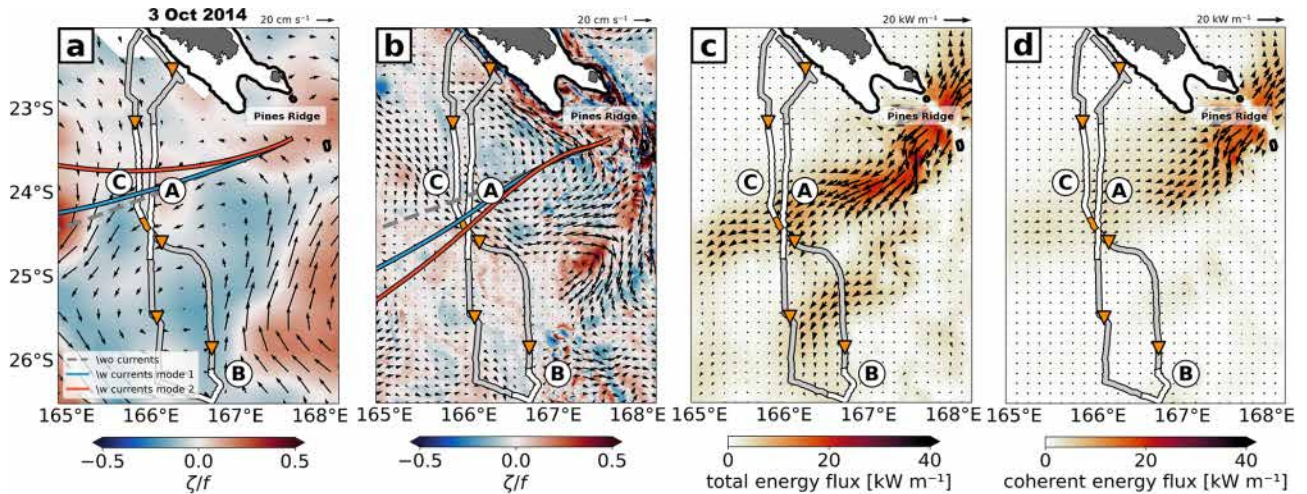
Figure 10. Same as Fig. 9, but for a daily-mean snapshot on 3 October 2014. Note that the semidiurnal energy flux underlies spring and neap tide variability, which explains the differences in the modeled coherent energy flux for different snapshots. The difference between the total and coherent energy flux can be associated with tidal incoherence.
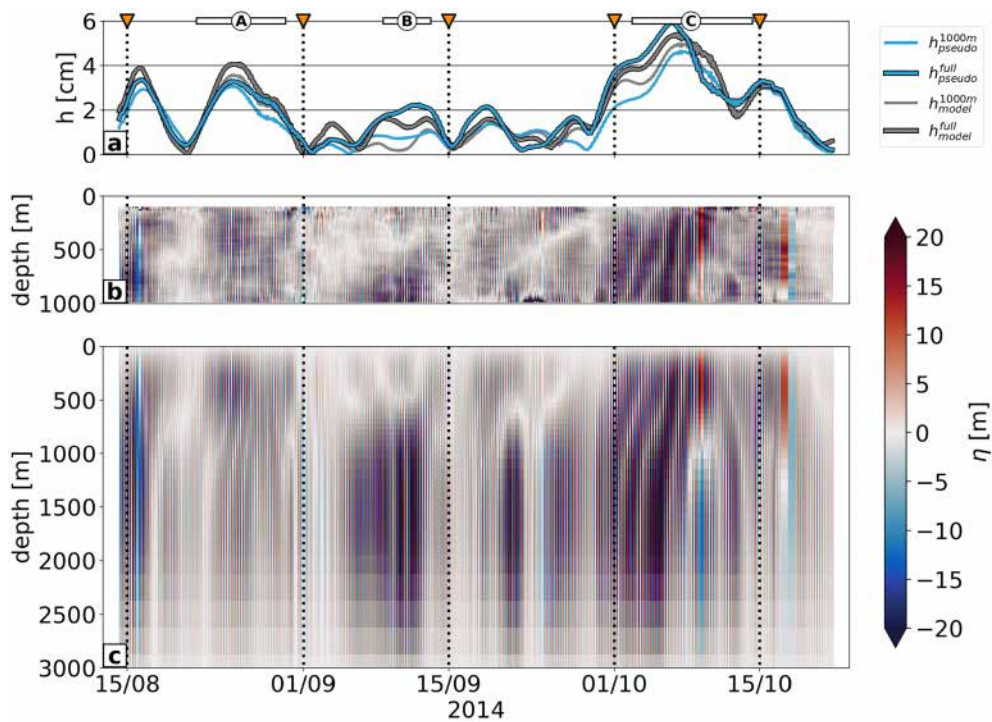

Figure 11. (a) Semidiurnal amplitude for the pseudo-glider steric height $h_{\mathrm{pseudo}}^{1000\,\mathrm{m}}$ (blue), the full-depth pseudo-glider steric height $h_{\mathrm{pseudo}}^{\mathrm{full}}$ (blue with black outlines), and the full-model steric height $h_{\mathrm{model}}^{1000\,\mathrm{m}}$ for the upper 1000 m (gray) and $h_{\mathrm{model}}^{\mathrm{full}}$ for the full-depth range (gray with black outlines). Here, we use a two-mode approximation to calculate $h_{\mathrm{pseudo}}^{\mathrm{full}}$. **(b)** Pseudo-glider vertical displacements $\eta_{\mathrm{pseudo}}^{1000\,\mathrm{m}}$ which are ultimately used to compute $h_{\mathrm{pseudo}}^{1000\,\mathrm{m}}$. **(c)** Pseudo-glider vertical displacements $\eta_{\mathrm{pseudo}}^{\mathrm{full}}$ extrapolated to the full depth using projections on climatological modes 1–2 which are ultimately used to compute $h_{\mathrm{pseudo}}^{\mathrm{full}}$.

The pseudo-glider steric height $\left(h_{\text{pseudo}}^{1000\text{m}} \right)$ follows the overall pattern of $h_{\text{model}}^{1000\text{m}}$ (Fig. 11a). However, it only accounts for 78 % of explained variance when referenced to $h_{\text{model}}^{\text{full}}$ (Table 1). This is, by construction, only due to the irregular glider sampling. Projecting the pseudo-glider vertical displacements onto climatological modes and extrapolating to the full-depth range can partly account for missing variance due to the glider sampling limited to the upper 1000 m (Fig. 11c). Using a two-mode approximation, we are able to increase the explained variance from 78 % $\left(h_{\text{pseudo}}^{1000\,\text{m}} \right)$ to 93 % ($h_{\text{pseudo}}^{\text{full}} \Sigma_{n=1}^2$; Table 1). From a qualitative perspective, this is also apparent in Fig. 11a, where $h_{\text{pseudo}}^{\text{full}}$ provides an overall improvement and compares better with $h_{\text{model}}^{\text{full}}$. Projecting on the two lowest modes gives the best result, although projecting on the first mode only increases the variance from 78 % to 85 % ($h_{\text{pseudo}}^{\text{full}} \Sigma_{n=1}^1$; Table 1).

4.5 How do the glider measurements compare with satellite altimetry?

Using a two-mode approximation, the methodology described in Sect. 3.6.1 and applied to the full-model pseudo glider in the previous section is now applied to the glider observations. The full-depth glider steric height $h_{\text{obs}}^{\text{full}}$ is compared to the empirical SSH estimates from HRET (see Sect. 2.4) to evaluate the spatiotemporal variability in the semidiurnal internal tide from a satellite altimetry point of view (Fig. 12). Note that in contrast to the glider observations, HRET represents exclusively the coherent tide. Within this context, we utilize HRET to reconstruct the semidiurnal signals composed of the M2 and S2 tides, for modes 1–2, prior to interpolating the resulting time series to align with the time stamps along the glider's track.

The overall spatiotemporal variability in the full-depth glider steric height corresponds well with HRET (Fig. 12a and c). Particularly, the spatiotemporal signals in the segments denoted as A and C are well captured, albeit reduced in amplitude (maximum 2 cm in HRET compared to maximum 4 cm in the glider observations). Good agreement is also seen for the signature from the middle to end of September. Contrarily, the distinct signal, denoted as B, which exhibits a surface signature of almost 4 cm in the glider observations is entirely absent in HRET.

Here, we build upon the full-depth steric height signal of the semidiurnal coherent internal tide, which sheds light on the coherent tide along the glider track (Fig. 12b). It corresponds to the full-depth glider steric height (Fig. 12a), suggestive of prevailing tidal coherence in the glider observations. Specifically, the tidal signature at B is also present, indicating at this location a potential misrepresentation of the coherent tide in HRET. This is not necessarily surprising considering that the glider sampling can access finer spatial scales. In contrast, the correct representation of the internal-

tide field in HRET is largely dependent on the available satellite tracks for a given area that are subject to a point-wise harmonic analysis, followed by a plane-wave fit in overlapping patches. Moreover, fine-scale features may be smoothed out due to the mapping technique applied in HRET (Zaron, 2019).

Despite apparent deviations in the spatiotemporal variability, it is noteworthy that the modal structures, specifically modes 1–2, match closely among in situ observations, numerical modeling, and altimetry. Among all the products, mode 1 predominates the signal, accounting for > 90 % of the baroclinic variance.

5 Summary and discussion

In situ observations from autonomous glider data have been previously exploited to infer internal-tide dynamics while providing important information on the spatial variability in high-frequency motion at fine spatial scales. Recent numerical modeling results have identified New Caledonia as a significant hot spot for internal-tide generation, characterized by the westward propagation of tidal energy within well-defined tidal beams (Bendinger et al., 2023).

In this study, we inferred internal tides from a glider survey carried out in the area south of New Caledonia in the southwestern tropical Pacific over the course of > 2 months. Spatiotemporal variability in the diurnal and semidiurnal internal tide is deduced by fitting a sinusoidal function on vertical isopycnal displacements using a least-squares method in 3 d running windows from the surface down to 1000 m depth. The glider observations suggest a pronounced dominance of the semidiurnal tide, which can explain locally up to 80 % of the total variance of the vertical displacements. This semidiurnal dominance is in agreement with the model results in Bendinger et al. (2023). Further, our analysis reveals distinct segments of elevated tidal activity expressed by semidiurnal isopycnal displacements exceeding 20 m.

Glider observations are combined with four-dimensional regional model output. This approach serves a dual purpose. First, glider observations assess the realism of internal-tide dynamics in the numerical simulation. Second, the four-dimensional regional model outputs are used to assess the glider's capability within the upper 1000 m to infer internal tides and to retrieve their associated SSH signature. To do so, we modeled the trajectory and sampling of a pseudo glider using the hourly output of the regional model linearly interpolated onto the glider time series with identical spatiotemporal sampling.

The observed spatiotemporal variability in the semidiurnal internal tide closely matches with the results of the pseudo glider, demonstrating an overall similarity in location, magnitude, and vertical structure of the tidal signatures. The previously performed tidal analysis in Bendinger et al. (2023) suggests that these signatures sampled by both the glider and

Table 1. Explained variability in $h_{\text{model}}^{1000\,\text{m}}$, $h_{\text{pseudo}}^{1000\,\text{m}}$, and $h_{\text{model}}^{\text{full}}$ using a first-mode approximation ($\Sigma_{n=1}^{1}$) and a two-mode approximation ($\Sigma_{n=1}^{2}$), referenced to $h_{\text{model}}^{\text{full}}$.

	$h_{\text{model}}^{1000\,\text{m}}$	$h_{\text{pseudo}}^{1000\,\text{m}}$	$h_{\text{pseudo}}^{\text{full}}\Sigma_{n=1}^{1}$	$h_{\text{pseudo}}^{\text{full}}\Sigma_{n=1}^{2}$
γ (cov(...,$h_{\text{model}}^{\text{full}}$)/var($h_{\text{model}}^{\text{full}}$)	0.91	0.78	0.85	0.93
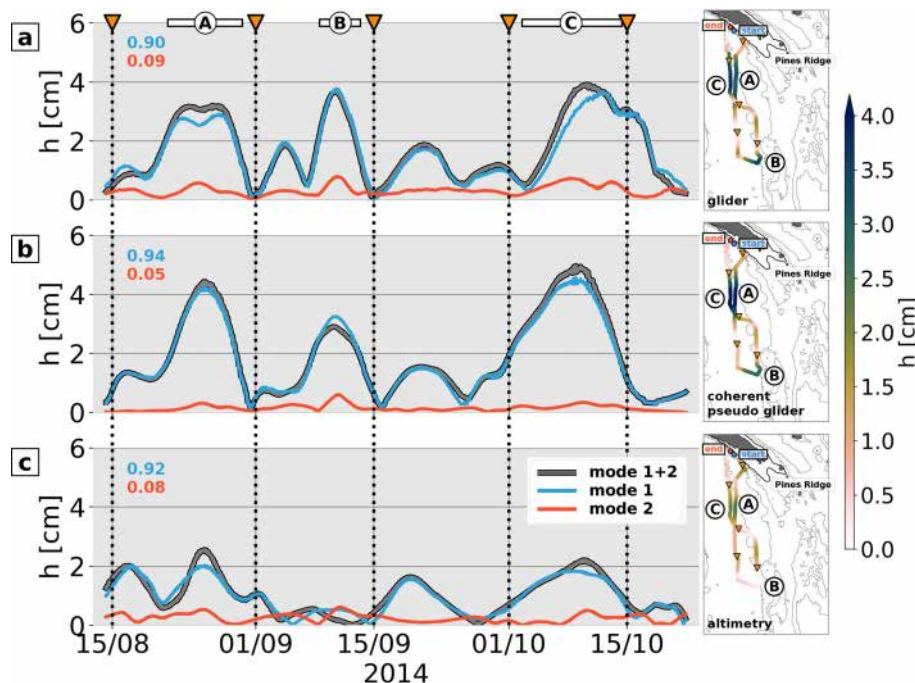
Figure 12. Semidiurnal amplitude along the glider track direction of **(a)** the full-depth glider steric height using a two-mode approximation $\left(h_{\text{obs}}^{\text{full}}\Sigma_{n=1}^{2}\right)$; **(b)** the full-depth coherent pseudo-glider steric height $h_{\text{coh}}^{\text{full}}$; and **(c)** HRET SSH for the baroclinic tide (gray with black outlines), mode 1 (blue), and mode 2 (red). The modal contributions of modes 1–2 are given in the upper-left corners. The right panels of **(a)**–**(c)** show the baroclinic amplitude along the glider track direction on a spatial map.

pseudo glider are associated with westward propagation of semidiurnal tidal energy, which can be traced back to the internal-tide generation south of New Caledonia.

We attribute the major discrepancies between glider observations and the full-model pseudo glider to tidal incoherence induced by eddy–internal-tide interactions. This is supported by a simplified ray-tracing analysis which tracks the propagation of a semidiurnal ray for a given initialization region and propagation angle. In the propagation direction, the semidiurnal ray may be refracted, associated with variations in phase velocity induced by the background currents of mesoscale eddies affecting the tidal ray orientation. Specifically, the theoretical pathway of the refracted tidal beam intersects with the glider track, coinciding with the location and time stamp where and when departure from tidal coherence is expected in the pseudo glider.

Using glider observations alone, a single glider mission is not sufficient to distinguish between tidal coherence and incoherence. Surely, repeated glider sections would provide

additional information on the coherent and incoherent variance while allowing for a model validation with more confidence. In any case, we note that the complementary analysis of in situ observations and numerical modeling can be used as a potential approach to infer where tidal incoherence may occur in glider observations, although this approach is limited to regions with available high-resolution model output including tidal forcing, which overlaps in space and time with glider data.

Through the vertical integration of vertical displacements, we established a connection between the semidiurnal internal tide's signature in the upper 1000 m and its expression in SSH. In the semidiurnal frequency band, the upper 1000 m in the pseudo-glider simulation accounts for 78 % of the full-depth steric height variance. To encompass the entire depth range of the semidiurnal tide, extending beyond 1000 m, we projected the pseudo glider's vertical displacements onto a set of climatological modes before extrapolating vertically. Utilizing a two-mode approximation, we increased the ex-

plained variance from 78 % to 93 % percent. When projecting on the first mode only, the explained variance increased to 85 %. Steric height, derived from the glider observations, shows good agreement with empirical SSH estimates from satellite altimetry, indicating the prevalence of tidal coherence during the glider mission. We point out that the methodology accounting for the full-depth range needs validation, especially in regions where high modes play a more significant role.

Linking interior dynamics of fine-scale physics with the expression in SSH has important implications for SWOT, as SWOT's SSH measurements encompass both balanced and unbalanced motions. In situ observations play a crucial role in disentangling the physical processes in the three-dimensional water column. We have demonstrated that gliders can serve as an effective in situ platform for extracting the SSH signature of internal tides, particularly in the area south of New Caledonia. This region became the focus of a dedicated in situ field campaign in boreal spring 2023, conducted within the framework of the SWOT AdAC consortium. The primary objective of this campaign was to comprehensively survey fine-scale physics, including internal tides, along two SWOT swaths during the fast-sampling phase. In an area of increased tidal activity, the SWOT observability of mesoscale and submesoscale dynamics may suffer from the dominance of unbalanced motion. For obvious reasons, the analyzed glider in this study cannot be used for the direct validation of SWOT.

Preliminary analyses using conventional satellite altimetry products have revealed the presence of multiple mesoscale eddies and frontal zones along the glider track direction. Future work will focus on the residual signal seen in Fig. 7c and the investigation of whether the glider observations corrected for the diurnal and semidiurnal tide can indeed be attributed to mesoscale and submesoscale dynamics (e.g., eddies and fronts), as suggested by satellite altimetry.

Review statement. This paper was edited by Rob Hall and reviewed by two anonymous referees.

References

Arbic, B. K.: Incorporating tides and internal gravity waves within global ocean general circulation models: A review, Prog. Oceanogr., 206, 102824, https://doi.org/10.1016/j.pocean.2022.102824, 2022.

Arbic, B. K., Alford, M. H., Ansong, J. K., Buijsman, M. C., Ciotti, R. B., Farrar, J. T., Hallberg, R. W., Henze, C. E., Hill, C. N., Luecke, C. A., Menemenlis, D., Metzger, E. J., Muller, M., Nelson, A. D., Nelson, B. C., Ngodock, H. E., Ponte, R. M., Richman, J. G., Savage, A. C., Scott, R. B., Shriver, J. F., Simmons, H. L., Souopgui, I., Timko, P. G., Wallcraft, A. J., Zamudio, L., and Zhao, Z.: Primer on global internal tide and internal gravity wave continuum modeling in HYCOM and MITgcm, New frontiers in Operational Oceanography, 307–392, https://doi.org/10.17125/gov2018.ch13, 2018.

Baines, P. G.: On internal tide generation models, Deep-Sea Res. Pt. I, 29, 307–338, https://doi.org/10.1016/0198-0149(82)90098-X, 1982.

Ballarotta, M., Ubelmann, C., Pujol, M.-I., Taburet, G., Fournier, F., Legeais, J.-F., Faugère, Y., Delepoulle, A., Chelton, D., Dibarboure, G., and Picot, N.: On the resolutions of ocean altimetry maps, Ocean Sci., 15, 1091–1109, https://doi.org/10.5194/os-15-1091-2019, 2019.

Bell Jr., T.: Topographically generated internal waves in the open ocean, J. Geophys. Res., 80, 320–327, https://doi.org/10.1029/JC080i003p00320, 1975.

Bendinger, A.: Internal tides vertical structure and steric sea surface height signature south of New Caledonia revealed by glider observations, Zenodo [data set], https://doi.org/10.5281/zenodo.12188295, 2024a.

Bendinger, A.: Internal tides vertical structure and steric sea surface height signature south of New Caledonia revealed by glider observations, Zenodo [software], https://doi.org/10.5281/zenodo.12188383, 2024b.

Bendinger, A., Cravatte, S., Gourdeau, L., Brodeau, L., Albert, A., Tchilibou, M., Lyard, F., and Vic, C.: Regional modeling of internal-tide dynamics around New Caledonia – Part 1: Coherent internal-tide characteristics and sea surface height signature, Ocean Sci., 19, 1315–1338, https://doi.org/10.5194/os-19-1315-2023, 2023.

Buijsman, M. C., Arbic, B. K., Richman, J. G., Shriver, J. F., Wallcraft, A. J., and Zamudio, L.: Semidiurnal internal tide incoherence in the equatorial p acific, J. Geophys. Res.-Oceans, 122, 5286–5305, https://doi.org/10.1002/2016JC012590, 2017.

Carter, G. S., Merrifield, M., Becker, J. M., Katsumata, K., Gregg, M., Luther, D., Levine, M., Boyd, T. J., and Firing, Y.: Energetics of M 2 barotropic-to-baroclinic tidal conversion at the Hawaiian Islands, J. Phys. Oceanogr., 38, 2205–2223, https://doi.org/10.1175/2008JPO3860.1, 2008.

CLS: Global Ocean Gridded L 4 Sea Surface Heights And Derived Variables Reprocessed 1993 Ongoing, E.U Copernicus Marine Service Information (CMEMS), Marine Data Store (MDS) [data set], https://doi.org/10.48670/moi-00148, 2023.

Debreu, L., Vouland, C., and Blayo, E.: AGRIF: Adaptive grid refinement in Fortran, Comput. Geosci., 34, 8–13, https://doi.org/10.1016/j.cageo.2007.01.009, 2008.

Duda, T. F., Lin, Y.-T., Buijsman, M., and Newhall, A. E.: Internal tidal modal ray refraction and energy ducting in baroclinic Gulf Stream currents, J. Phys. Oceanogr., 48, 1969–1993, https://doi.org/10.1175/JPO-D-18-0031.1, 2018.

Durand, F., Marin, F., Fuda, J.-L., and Terre, T.: The east caledonian current: a case example for the intercomparison between altika and in situ measurements in a boundary current, Mar. Geodesy, 40, 1–22, https://doi.org/10.1080/01490419.2016.1258375, 2017.

d'Ovidio, F., Pascual, A., Wang, J., Doglioli, A. M., Jing, Z., Moreau, S., Grégori, G., Swart, S., Speich, S., Cyr, F., Legresy, B., Chao, Y., Fu, L., and Morrow, R.: Frontiers in fine-scale in situ studies: Opportunities during the SWOT fast sampling phase, Front. Mar. Sci., 6, 168, https://doi.org/10.3389/fmars.2019.00168, 2019.

Fu, L.-L., Alsdorf, D., Morrow, R., Rodriguez, E., and Mognard, N.: SWOT: the Surface Water and Ocean Topography Mission: wide-swath altimetric elevation on Earth, Tech. rep., Pasadena, CA: Jet Propulsion Laboratory, National Aeronautics and Space, http://hdl.handle.net/2014/41996 (last access: 16 May 2023), 2012.

Ganachaud, A., Cravatte, S., Melet, A., Schiller, A., Holbrook, N., Sloyan, B., Widlansky, M., Bowen, M., Verron, J., Wiles, P., Ridway, K., Sutton, P., Sprintall, J., Steinberg, C., Brassington, G., Cai, W., Davis, R., Gasparin, F., Gourdeau, L., Hasegawa, T., Kessler, W., Maes, C., Takahashi, K., Richards, K. J., and Send, U.: The Southwest Pacific Ocean circulation and climate experiment (SPICE), J. Geophys. Res.-Oceans, 119, 7660–7686, https://doi.org/10.1002/2013JC009678, 2014.

Gill, A. E.: Atmosphere-ocean dynamics, vol. 30, Academic press, ISBN: 9780122835223, 1982.

Guo, Z., Wang, S., Cao, A., Xie, J., Song, J., and Guo, X.: Refraction of the M2 internal tides by mesoscale eddies in the South China Sea, Deep-Sea Res. Pt. I, 192, 103 946, https://doi.org/10.1016/j.dsr.2022.103946, 2023.

Hall, R. A., Aslam, T., and Huvenne, V. A.: Partly standing internal tides in a dendritic submarine canyon observed by an ocean glider, Deep-Sea Res. Pt. I, 126, 73–84, https://doi.org/10.1016/j.dsr.2017.05.015, 2017.

Hall, R. A., Berx, B., and Damerell, G. M.: Internal tide energy flux over a ridge measured by a co-located ocean glider and moored acoustic Doppler current profiler, Ocean Sci., 15, 1439–1453, https://doi.org/10.5194/os-15-1439-2019, 2019.

Hersbach, H., Bell, B., Berrisford, P., Hirahara, S., Horányi, A., Muñoz-Sabater, J., Nicolas, J., Peubey, C., Radu, R., Schepers, D., Simmons, A., Soci, C., Abdalla, S., Abellan, X., Balsamo, G., Bechtold, P., Biavati, G., Bidlot, J., Bonavita, M., De Chiara, G., Dahlgren, P., Dee, D., Diamantakis, M., Dragani, R., Flemming, J., Forbes, R., Fuentes, M., Geer, A., Haimberger, L., Healy, S., Hogan, R. J., Hólm, E., Janisková, M., Keeley, S., Laloyaux, P., Lopez, P., Lupu, C., Radnoti, G., de Rosnay, P., Rozum, I., Vamborg, F., Villaume, S., and Thépaut, J.-N.: The ERA5 global reanalysis, Q. J. Roy. Meteor. Soc., 146, 1999–2049, https://doi.org/10.1002/qj.3803, 2020.

Johnston, T. S. and Rudnick, D. L.: Trapped diurnal internal tides, propagating semidiurnal internal tides, and mixing estimates in the California Current System from sustained glider

observations, 2006–2012, Deep-Sea Res. Pt. II, 112, 61–78, https://doi.org/10.1016/j.dsr2.2014.03.009, 2015.

Johnston, T. S., Rudnick, D. L., Alford, M. H., Pickering, A., and Simmons, H. L.: Internal tidal energy fluxes in the South China Sea from density and velocity measurements by gliders, J. Geophys. Res.-Oceans, 118, 3939–3949, https://doi.org/10.1002/jgrc.20311, 2013.

Johnston, T. S., Rudnick, D. L., and Kelly, S. M.: Standing internal tides in the Tasman Sea observed by gliders, J. Phys. Oceanogr., 45, 2715–2737, https://doi.org/10.1175/JPO-D-15-0038.1, 2015.

Keppler, L., Cravatte, S., Chaigneau, A., Pegliasco, C., Gourdeau, L., and Singh, A.: Observed characteristics and vertical structure of mesoscale eddies in the southwest tropical Pacific, J. Geophys. Res.-Oceans, 123, 2731–2756, https://doi.org/10.1002/2017JC013712, 2018.

Kerry, C. G., Powell, B. S., and Carter, G. S.: The impact of subtidal circulation on internal tide generation and propagation in the Philippine Sea, J. Phys. Oceanogr., 44, 1386–1405, https://doi.org/10.1175/JPO-D-13-0142.1, 2014.

Locarnini, M., Mishonov, A., Baranova, O., Boyer, T., Zweng, M., Garcia, H., Seidov, D., Weathers, K., Paver, C., and Smolyar, I.: World ocean atlas 2018, volume 1: Temperature, NOAA Atlas NESDIS 81, 52 pp., https://archimer.ifremer.fr/doc/00651/76338/ (last access: 27 February 2023), 2018.

Lyard, F. H., Allain, D. J., Cancet, M., Carrère, L., and Picot, N.: FES2014 global ocean tide atlas: design and performance, Ocean Sci., 17, 615–649, https://doi.org/10.5194/os-17-615-2021, 2021.

Merrifield, M. A. and Holloway, P. E.: Model estimates of M2 internal tide energetics at the Hawaiian Ridge, J. Geophys. Res.-Oceans, 107, 5–1, https://doi.org/10.1029/2001JC000996, 2002.

Merrifield, M. A., Holloway, P. E., and Johnston, T. S.: The generation of internal tides at the Hawaiian Ridge, Geophys. Res. Lett., 28, 559–562, https://doi.org/10.1029/2000GL011749, 2001.

Morrow, R., Fu, L.-L., Ardhuin, F., Benkiran, M., Chapron, B., Cosme, E., d'Ovidio, F., Farrar, J. T., Gille, S. T., Lapeyre, G., Le Traon, P.-Y., Pascual, A., Ponte, A., Qiu, B., Rascle, N., Ubelmann, C., Wang, J., and Zaron, E. D.: Global observations of fine-scale ocean surface topography with the Surface Water and Ocean Topography (SWOT) mission, Front. Mar. Sci., 6, 232, https://doi.org/10.3389/fmars.2019.00232, 2019.

Nash, J. D., Kelly, S. M., Shroyer, E. L., Moum, J. N., and Duda, T. F.: The unpredictable nature of internal tides on continental shelves, J. Phys. Oceanogr., 42, 1981–2000, https://doi.org/10.1175/JPO-D-12-028.1, 2012.

Park, J.-H. and Watts, D. R.: Internal tides in the southwestern Japan/East Sea, J. Phys. Oceanogr., 36, 22–34, https://doi.org/10.1175/JPO2846.1, 2006.

Rainville, L. and Pinkel, R.: Propagation of low-mode internal waves through the ocean, J. Phys. Oceanogr., 36, 1220–1236, https://doi.org/10.1175/JPO2889.1, 2006.

Rainville, L., Lee, C. M., Rudnick, D. L., and Yang, K.-C.: Propagation of internal tides generated near Luzon Strait: Observations from autonomous gliders, J. Geophys. Res.-Oceans, 118, 4125–4138, https://doi.org/10.1002/jgrc.20293, 2013.

Ray, R. D. and Zaron, E. D.: M2 internal tides and their observed wavenumber spectra from satellite altimetry, J. Phys. Oceanogr., 46, 3–22, https://doi.org/10.1175/JPO-D-15-0065.1, 2016.

Ridgway, K., Dunn, J., and Wilkin, J.: Ocean interpolation by four-dimensional weighted least squares–Application to the waters around Australasia, J. Atmos. Ocean. Technol., 19, 1357–1375, https://doi.org/10.1175/1520-0426(2002)019<1357:OIBFDW>2.0.CO;2, 2002 (data set available at http://www.marine.csiro.au/~dunn/cars2009/, last access: 21 February 2021).

Rudnick, D. L.: Ocean research enabled by underwater gliders, Annu. Rev. Mar. Sci., 8, 519–541, https://doi.org/10.1146/annurev-marine-122414-033913, 2016.

Rudnick, D. L. and Cole, S. T.: On sampling the ocean using underwater gliders, J. Geophys. Res.-Oceans, 116, C08010, https://doi.org/10.1029/2010JC006849, 2011.

Sérazin, G., Marin, F., Gourdeau, L., Cravatte, S., Morrow, R., and Dabat, M.-L.: Scale-dependent analysis of in situ observations in the mesoscale to submesoscale range around New Caledonia, Ocean Sci., 16, 907–925, https://doi.org/10.5194/os-16-907-2020, 2020.

Smith, W. H. F. and Sandwell, D. T.: Global sea floor topography from satellite altimetry and ship depth soundings, Science, 277, 1956–1962, https://doi.org/10.1126/science.277.5334.1956, 1997.

Smith, K. S. and Vallis, G. K.: The scales and equilibration of midocean eddies: Freely evolving flow, J. Phys. Oceanogr., 31, 554–571, https://doi.org/10.1175/1520-0485(2001)031<0554:TSAEOM>2.0.CO;2, 2001.

Testor, P., De Young, B., Rudnick, D. L., Glenn, S., Hayes, D., Lee, C. M., Pattiaratchi, C., Hill, K., Heslop, E., Turpin, V., Alenius, P., Barrera, C., Barth, J. A., Beaird, N., Bécu, G., Bosse, A., Bourrin, F., Brearley, J. A., Chao, Y., Chen, S., Chiggiato, J., Coppola, L., Crout, R., Cummings, J., Curry, B., Curry, R., Davis, R., Desai, K., DiMarco, S., Edwards, C., Fielding, S., Fer, I., Frajka-Williams, E., Gildor, H., Goni, G., Gutierrez, D., Haugan, P., Hebert, D., Heiderich, J., Henson, S., Heywood, K., Hogan, P., Houpert, L., Huh, S., Inall, M. E., Ishii, M., Ito, S., Itoh, S., Jan, S., Kaiser, J., Karstensen, J., Kirkpatrick, B., Klymak, J., Kohut, J., Krahmann, G., Krug, M., McClatchie, S., Marin, F., Mauri, E., Mehra, A., Meredith, M. P., Meunier, T., Miles, T., Morell, J. M., Mortier, L., Nicholson, S., O'Callaghan, J., O'Conchubhair, D., Oke, P., Pallàs-Sanz, E., Palmer, M., Park, J., Perivoliotis, L., Poulain, P.-M., Perry, R., Queste, B., Rainville, L., Rehm, E., Roughan, M., Rome, N., Ross, T., Ruiz, S., Saba, G., Schaeffer, A., Schönau, M., Schroeder, K., Shimizu, Y., Sloyan, B. M., Smeed, D., Snowden, D., Song, Y., Swart, S., Tenreiro, M., Thompson, A., Tintore, J., Todd, R. E., Toro, C., Venables, H., Wagawa, T., Waterman, S., Watlington, R. A., and Wilson, D.: OceanGliders: a component of the integrated GOOS, Front. Mar. Sci., 6, 422, https://doi.org/10.3389/fmars.2019.00422, 2019.

Vic, C., Garabato, A. C. N., Green, J. M., Spingys, C., Forryan, A., Zhao, Z., and Sharples, J.: The lifecycle of semidiurnal internal tides over the northern Mid-Atlantic Ridge, J. Phys. Oceanogr., 48, 61–80, https://doi.org/10.1175/JPO-D-17-0121.1, 2018.

Zaron, E. D.: Mapping the nonstationary internal tide with satellite altimetry, J. Geophys. Res.-Oceans, 122, 539–554, https://doi.org/10.1002/2016JC012487, 2017.

Zaron, E. D.: Baroclinic tidal sea level from exact-repeat mission altimetry, J. Phys. Oceanogr., 49, 193–210, https://doi.org/10.1175/JPO-D-18-0127.1, 2019 (data available

at: https://ingria.ceoas.oregonstate.edu/~zarone/downloads.html, last access: 12 September 2022).

Zhao, Z., Alford, M. H., MacKinnon, J. A., and Pinkel, R.: Long-range propagation of the semidiurnal internal tide from the Hawaiian Ridge, J. Phys. Oceanogr., 40, 713–736, https://doi.org/10.1175/2009JPO4207.1, 2010.

Zhao, Z., Alford, M. H., Girton, J. B., Rainville, L., and Simmons, H. L.: Global observations of open-ocean mode-1 M2 internal tides, J. Phys. Oceanogr., 46, 1657–1684, https://doi.org/10.1175/JPO-D-15-0105.1, 2016.

Zilberman, N., Merrifield, M., Carter, G., Luther, D., Levine, M., and Boyd, T. J.: Incoherent nature of M 2 internal tides at the Hawaiian Ridge, J. Phys. Oceanogr., 41, 2021–2036, https://doi.org/10.1175/JPO-D-10-05009.1, 2011.

Zweng, M., Seidov, D., Boyer, T., Locarnini, M., Garcia, H., Mishonov, A., Baranova, O., Weathers, K., Paver, C., and Smolyar, I.: World ocean atlas 2018, volume 2: Salinity, NOAA Atlas NESDIS 82, 50 pp., https://archimer.ifremer.fr/doc/00651/76339/ (last access: 27 February 2023), 2019.